JOURNAL OF MATERIALS SCIENCE **35** (2000) 1115–1124

Residual stress and damage effect on integrity of ground silicon nitride

R. W. MONAHAN, BI ZHANG, FULUN YANG, JIEXIN WANG, ZHENQI ZHU*
Department of Mechanical Engineering, Advanced Technology Institute, University of Connecticut, Storrs, Connecticut, 06269, USA
E-mail: monahan@neca.com

Ceramic workpiece integrity and residual surface stresses generated by single pass diamond grinding were evaluated for three flaring cup wheels and four machine-loop stiffnesses. Stresses in silicon nitride bars ground on one face were characterized by X-ray diffraction, strength by four-point bending, and grinding damage depth by scanning electron microscopy. A custom-built workpiece holder was used to tune the grinding machine-loop stiffness. Electrolytic in-process dressing was applied to one of the wheels to provide stable cutting conditions. The experimental results indicate machine stiffness does not have significant influence on flexural strength, but rather affects the depth of cut. All ground surfaces have some degree of damage and residual stress, and differences are revealed between wheel bonds and grit sizes. The competing phenomena of strength enhancement due to residual stress and strength degradation due to damage are discussed.

1. Introduction

Fixed diamond abrasive grinding is widely studied and applied to produce ceramic components of high quality in terms of form and finish accuracy. While these features are often of primary concern, the processing conditions and final workpiece integrity may be equally important. To economically produce and improve the reliability of brittle materials, the machine dynamics and grinding conditions as well as the resulting workpiece state of stress, subsurface damage and strength should be considered. The fundamental objective of a grinding process is to achieve the maximum possible material removal rate while maintaining sufficient material integrity and dimensional accuracy.

The material removal mechanism in grinding brittle materials involves localized contacts that cause irreversible inhomogeneous deformation and fracture. This process leads to machined components that often contain a deformed layer, surface and subsurface microcracks, material pulverization, smeared areas, phase transformation regions, and other types of surface and subsurface damage [1–8]. This damage is the origin of both compressive and tensile residual stresses. It is well postulated that isolated elastic-plastic contact gives rise to a radially compressive residual stress field, with a corresponding locally tangent tensile residual stress field outside the plastic zone which surrounds the contact site. Strength-degrading cracks form on median planes within the local tensile stress field. Overlapping residual stress fields from adjacent damage sites in the ground surface form a layer of residual compressive stress. This compression tends to reduce, but does not eliminate, the residual tensile stress acting on the strength-controlling flaw [8].

Residual stresses in ceramic materials have long been recognized as having a significant influence on mechanical behavior and surface integrity [8–12]. Compressive residual stresses can enhance the strength of a specimen, in contrast to tensile residual stresses. Additionally, studies have shown that grinding-induced damage can be detrimental to the strength and thus the performance of ceramic parts [13–16]. The extent and nature of machining-induced damage resulting in workpiece strength reduction can strongly depend on the process parameters, for example the machine dynamics, grit depth of cut, or abrasive grit size [13, 17–24]. Furthermore, the extent of strength reduction is also related to the material properties, e.g. microstructure, grain size or fracture toughness [3, 12, 25–27].

Accounting for the process conditions and material properties, the strength of a ground ceramic workpiece depends on the baseline material strength and the competing phenomena of strength enhancement due to residual stress and strength degradation due to damage. Therefore, the strength σ may be expressed as $\sigma = \sigma_b + \Delta\sigma_c - \Delta\sigma_d$, where σ_b is the baseline workpiece strength; $\Delta\sigma_c$ is the strength gain through the introduction of compressive residual stresses; $\Delta\sigma_d$ is the strength loss due to grinding damage. Under normal grinding conditions, the superposition of strength gain due to $\Delta\sigma_c$ and strength loss due to $\Delta\sigma_d$ occurs simultaneously, which makes predicting ground workpiece

* *Present address*: Stevens Institute of Technology, Department of Mechanical Engineering, Hoboken, NJ 07030.

strength σ difficult. This suggests that both residual stress and damage measurements are required to predict workpiece strength.

Several researchers have shown that surface grinding transverse to the tensile stress direction in bars subjected to four-point bending results in a lower strength compared to grinding in the longitudinal direction [13, 15, 19, 27]. Rice [27] reported that strength anisotropy, with reference to grinding direction, was higher for finer-grain materials. Strakna *et al.* [15] showed grinding conditions did not affect the strength in longitudinal direction; however, strength was reduced when grinding was performed in the transverse direction as the volumetric material removal rate was increased by a factor of 30.

Nondestructive and destructive approaches have been explored to assess damage in ceramics induced by a machining process. Ahn *et al.* [28] used an ultrasonic technique to detect subsurface lateral cracks in silicon nitride subjected to diamond indentation. A thermal wave measurement technique was also investigated. Both of these methods were successful in detecting cracks, but were less successful in detecting damage depth.

In order to directly observe subsurface damage, destructive techniques are likely required. Yoshikawa *et al.* [5], and Zhang and Howes [6, 7] used four methods to characterize damage induced by a single-point diamond for several ceramics. The slicing, etching, fracture and taper polishing methods were claimed to be equally effective for multiple-point diamond grinding. A different technique was used by Xu and Jahnmir [29], where an adhesive was used to mate the polished faces of two specimens prior to grinding, leaving approximately 1 μm between each specimen. After machining, the specimens were separated and optically viewed to identify subsurface damage.

Perhaps the most common method for evaluating machining effects on the strength of brittle materials is a bending test, where the surface of interest is subjected to tensile stress in bending. Using this technique, many investigators have assessed the effects of various grinding parameters and conditions on the bending strength of ceramics [12, 13, 15, 19, 20, 30].

The objective of this experimental study was to characterize the competing phenomena of strength enhancement due to residual stress and strength degradation due to damage for high pressure sintered silicon nitride (HPSSN) ground using flaring cup diamond wheels under several conditions. Three wheels were used, enabling two mean grit sizes and two bond types to be evaluated. Grinding was done in the transverse direction (using longitudinal feed) relative to the stress direction used in four-point bending tests. Results for four machine stiffnesses and two set depths of cut are reported. Residual surface stresses are characterized by X-ray diffraction. Surface finish measurements were done with a profilometer, and a standard four-point bending test was used to measure the workpiece transverse bending strength. After the strength tests, the largest remaining workpiece sections were taper lapped to ascertain the mean subsurface grinding damage using scanning electron microscopy (SEM). In addition, several samples were etched in hydrofluoric acid to observe the grinding damage.

2. Experimental procedure

All grinding tests were conducted on a precision grinding machine (Dover Instrument Corporation, Model 956-S) capable of achieving sub-micron tolerances. The vertical-spindle machine had a granite base and column to support the X-Y-Z aerostatic table and aerostatic spindle respectively. A closed-loop laser interferometer system provided a 75 nm slideway positioning resolution in the X, Y and Z-directions. The spindle axial run-out was 0.05 μm and the slide straightness error was 0.01 μm over 25 mm.

Single pass grinding was used on the HPSSN (Allied Signal Inc., GS-44) workpieces. Additional properties for the single phase polycrystalline material are shown in Table I. Two set depths of cut (SDOC) and four machine stiffnesses were used for each wheel. The approach used in this study was to select an SDOC and vary only the machine stiffness. In this way the actual depth of cut (ADOC), and hence the stock removal rate, changed with machine stiffness. This approach was selected to observe the static and dynamic responses of the machine for a given input (SDOC). The post grinding measurements reported are surface finish, bending strength, surface residual stress and damage depth.

2.1. Grinding process configuration

A unique aspect of this research was the application of the compliant workpiece holder shown in Fig. 1.

TABLE I S_3N_4 properties (Apllied Signal, GS-44)

Density	3.2 g/cm^3
Elastic modulus	300 GPa
Flexural strength	1 051 MPa (ambient) 655 MPa at 1,100°C
Fracture toughness	8.25 MPa·m$^{1/2}$
Max. use temperature	1100°C
Poisson's ratio	0.27
Thermal conductivity	35 W/m·K
Thermal expansion	3.4×10^{-6}/°C (20–1,000°C)
Vickers hardness	14.6 GPa
Size, final (L × W × H)	45 × 4 × 3 mm

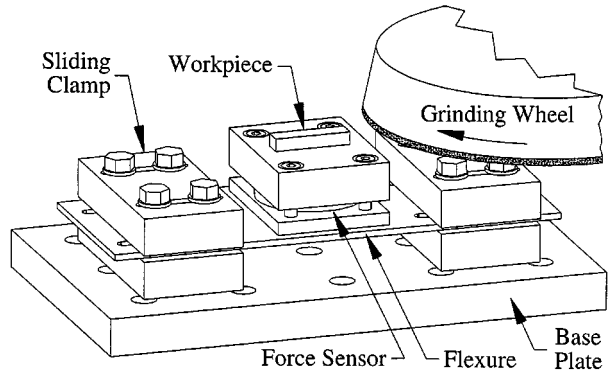

Figure 1 Adjustable-compliance workpiece holder.

The motivation for designing and using such a holder was to isolate the effect of machine stiffness for a given grinding cycle. This approach eliminates the influences of motion errors and positioning characteristics that would result if different machines were used. The holder design incorporates sliding clamps to fix the ends of a 3 mm thick flexure. The compliance of the holder was tuned by adjusting the distance between the sliding blocks. For the grinding tests, the workpiece holder was tuned to stiffnesses of 5, 10, 20 and 40 N/μm. The grinding forces were measured using an integrated three-axis piezoelectric force transducer (Kistler, Model 9167A1.5) mounted between the flexure and the workpiece mounting block. The force signal was digitized at a rate of 500 Hz for the grinding tests.

The pseudo-static machine-loop stiffness was measured using the integrated force transducer, a piezoelectric actuator (Physik Intrumente, P-841), and capacitance displacement sensors (Lion Precision). The actuator was located between the workpiece mounting block and the abrasive rim of the cup grinding wheel. The highest measured structural-loop stiffness was 100 N/μm , where the applied force was 80 N and the measured displacement was 0.8 μm. An impulse response test was performed under 10, 20 and 40 N/μm stiffness conditions using the same setup as the static stiffness tests. The respective natural frequencies were 60, 75 and 80 Hz.

Two of the three flaring cup diamond grinding wheels (Type 11A2) used had vitrified bonds and the third was a cast iron fiber bond (CIFB). The outer diameter of each wheel was 180 mm with an abrasive rim 5 mm wide. The diamond abrasive for each wheel was friable. Additional wheel specifications are given in Table II, where the abbreviated wheel designations used below are shown in parentheses. Note that the 1000-C wheel complies with the Japanese standard, which is equivalent to a U.S. standard mesh size of 600. The maximum axial runout for all the grinding wheels was 2 μm. The cutting fluid used was a synthetic, water soluble solution (ITW Fluid Products Group, Rustlick G-10066D) that was delivered through a heat exchanger.

A silicon carbide wheel brake-truer was applied to each wheel prior to grinding. Alumina dressing sticks were used for the vitrified bond wheels and a commercial electrolytic in-process dressing (ELID) system (Fuji Elider, ED-910) was used for the CIFB wheel. A custom-made copper electrode was designed and manufactured to enhance the electrolytic conductivity. A square pulse wave with a 2 μs on/off time was used with an open voltage of 60 V and peak current was 10 A for the ELID system. Before the grinding tests, each wheel was subjected to grinding a cast iron block to stabilize the wheel surface. The wheel was considered stable when the grinding forces became steady.

Five workpieces were used for each grinding condition, where the wheel surface speed was 24 m/s (2,500 RPM) and the table feed rate was 5 mm/s. The final dimension of each workpiece was approximately $45 \times 4 \times 3$ mm. Two SDOCs were used in this study, 10 μm and 25 μm. These SDOCs yield specific stock removal rates of $Q'_w = 2.4$ mm^3/(min·mm) and $Q'_w = 6.0$ mm^3/(min·mm) respectively. The stock removal rates were calculated neglecting deflection and using a workpiece width of 4 mm. The specific stock removal rates were obtained assuming the grinding wheel spindle was vertical and the wheel width was 5 mm. All of the above conditions were used for each wheel with the exception of the 600-V wheel. The grinding machine motor lacked the necessary power to maintain the wheel speed at an SDOC of 25 μm.

The ADOC was experimentally measured using the integrated workholder force sensor and the grinding machine's laser interferometer. One grinding pass was made at a fixed depth of cut, and the grinding wheel was then withdrawn. The ground surface was located by slowly feeding in the wheel while monitoring the force signal for fluctuations indicating contact with the workpiece. The reported specific stock removal rates were calculated based on these ADOC measurements.

2.2. Post grinding measurements

Surface roughness (R_a) measurements were made in the longitudinal direction (feed direction) with a surface profilometer (Federal Products Corporation, Surfanalyzer 5000). Longitudinal residual stresses were obtained using X-ray diffraction (Philips, Model PW 1835) with chromium-K$_\alpha$ radiation. Additional measurement conditions are shown in Table III. The effective X-ray penetration depth was 25 μm, based on the reduction of the primary incident beam intensity to 37% (e.g., $1/e$%) of its initial value [11]. The $\sin^2 \Psi$ method was used to determine the residual stresses. The workpiece strength was measured using a hydraulic material test machine (Instron Corp., Model 8511) with a four-point bending fixture per standard guidelines of

TABLE II Flaring cup diamond grinding wheel specifications

Grinding wheel	Bond type	Mesh no.	Mean grit size	Wheels dressing
SD120N100V[a] (120-V)[b]	Vitrified	120	125 μm	Alumina Stick
SD600N100V[a] (600-V)[b]	Vitrified	600	15 μm	Alumina Stick
SD1000N100C[c] (1000-C)[b]	Cast-Iron-Fiber	1000 (Japanese)	15 μm	ELID

[a]Norton Company.
[b]Abbreviations for grinding wheel designations used in the text.
[c]Fuji Die Company.

TABLE III Residual Stress X-ray measurement conditions

Radiation	Cr-K$_\alpha$ spectrum
Radiation wavelength	0.2291 nm
Mono-chrometer setting	Cr-K$_\alpha$
Diffraction plane (hkl)	β-Si_3N_4 (321)
Tube voltage	40 V
Tube current	35 A
Bragg angle	118.25°
Ψ angles scanned	−40°, −25°, −10°, 0°, 15°, 30°, 45°
Data points per Ψ angle	250
Step size	0.02°
Scanning speed	0.3°/min

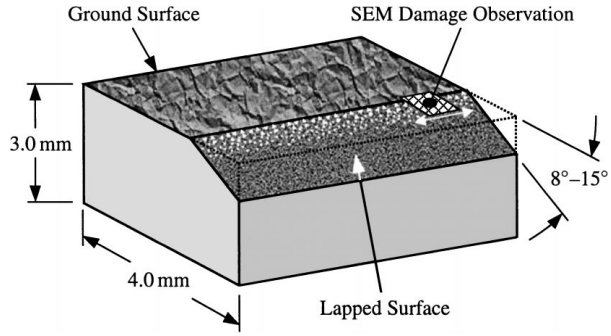

Figure 2 Lapped workpiece showing SEM observation area.

the American Society for Testing Materials (ASTM) C1161-94 Configuration B [31]. It should be pointed out the Weibull statistics are not reported because an inadequate number of bending tests (five) were performed for each grinding condition.

An SEM (Jeol, Model JSM 840A) was used to assess subsurface damage induced by the grinding process. After performing bending tests, the largest remaining specimen piece was selected for the damage depth measurements. Each specimen was prepared by taper lapping a portion of the ground surface, along the specimen length, at a small angle relative to the ground surface plane as shown in Fig. 2. Various lapping angles were used in the range of 8–15°. The lapping process consisted of four stages, using progressively smaller free diamond abrasives. The abrasive grit sizes were 6–12 μm, 2–4 μm, 1–2 μm and 0–0.25 μm. Preparing the specimens in this way generated a gradual transition between the ground surface (damaged) and lapped surface (bulk material).

Fig. 2 illustrates how the transition region between the ground and lapped surfaces was viewed using SEM. A magnification of 1000× was used, which provided a viewable screen image (frame) of approximately 110 μm wide. By traversing along the transition region frame-by-frame, 99–170 damage measurements were made for each workpiece depending on the specimen length. The measurements were made using a scale on the SEM screen to an accuracy of ± 1 mm, which corresponds to ± 0.63 μm accuracy for each damage depth measurement.

One concern in assessing the damage depth is determining the location of the reference edge between the ground and lapped surfaces. Three criteria were used. First, if the edge transition was apparent, it was extended horizontally to the next frame and subsequent frames. Second, the ends of apparent micro-scratches resulting from the lapping process were used to indicate the end of the lapped surface. Finally, significant changes in the uniformity or appearance of the ground surfaces were taken to indicate the end of the ground surface.

Another issue was determining the difference between grinding-induced damage, a material characteristic, and a lapping-process artifact. This issue was addressed once the transition reference line was established for a given frame. If a geometric pattern (void, pit or crack) appeared to extend from the ground surface into the lapped surface it was considered damage. If a pattern extended from the lapped surface into the ground surface and terminated near the transition reference line within the ground surface, it was not considered damage and was assumed to be an artifact from the lapping process. Once these patterns were evaluated for a given frame, the pattern extending farthest from the reference line (perpendicular) into the lapped surface was measured and considered the component of damage depth for that frame. The mean damage depths for each workpiece were calculated based on the measured lapped angle as shown in Fig. 2. This angle was measured using an optical comparator to within $\pm 1/2°$.

3. Results and discussion

The following sections present and discuss the experimental data for each of the three wheels tested. Five workpieces were used for each grinding condition, where two SDOCs and four machine stiffnesses were used for each wheel, with the exception of the 600-V wheel as noted above. In addition, no data was collected for the 120-V wheel for 20 N/μm machine stiffness and SDOC = 10 μm. The measured (actual) specific material removal rates (mm^3/(min·mm)) are indicated next to the respective data points on the charts that follow. The filled family of symbols are for an SDOC of 10 μm and the open symbols are for 25 μm SDOC.

3.1. Machine stiffness and grinding forces

Fig. 3 shows how machine-loop stiffness affects the normal grinding force F_{sn}, where F_{sn} is the mean value measured during steady-state grinding. In general, as the machine stiffness is increased a corresponding increase in F_{sn} is realized. This results in a larger ADOC and correspondingly higher stock removal rate. It should be pointed out that the threshold grinding forces were considered constant for each wheel because consistent wheel truing/dressing was performed before each workpiece was ground.

The 600-V wheel produced the highest F_{sn} compared to the 120-V and 1000-C wheels at a 10 μm SDOC. Although both the 600-V and 1000-C wheels have a mean grit size of 15 μm, the F_{sn} is nearly double for the same SDOC at each machine stiffness. Further, the specific stock removal rates for the 600-V wheel were consistently lower, indicating the 1000-C wheel acted sharper. This is explained by the use of the ELID system applied with the 1000-C wheel. ELID maintains the wheel sharpness (condition) throughout the grinding cycle thereby yielding a lower F_{sn} and higher removal rate.

The influence of ELID is further revealed by comparing the 120-V wheel in Fig. 3a, mean grit size of 125 μm, and the 1000-C wheel in Fig. 3b. One would expect F_{sn} to be significantly higher for the smaller grit grinding wheel used at the same SDOC. However, both F_{sn} and the stock removal rates are comparable but slightly lower for the 1000-C wheel under each test condition.

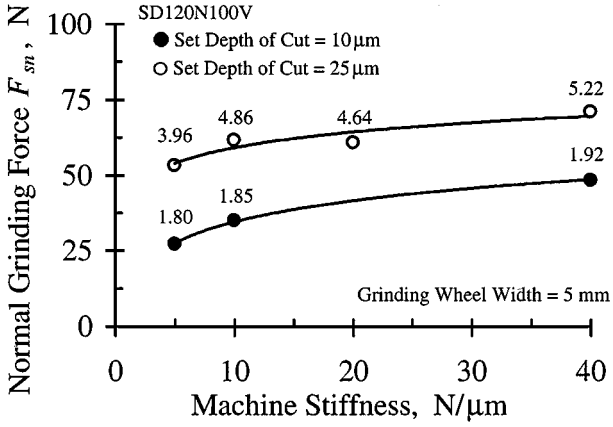

(a) SD120N100V wheel.

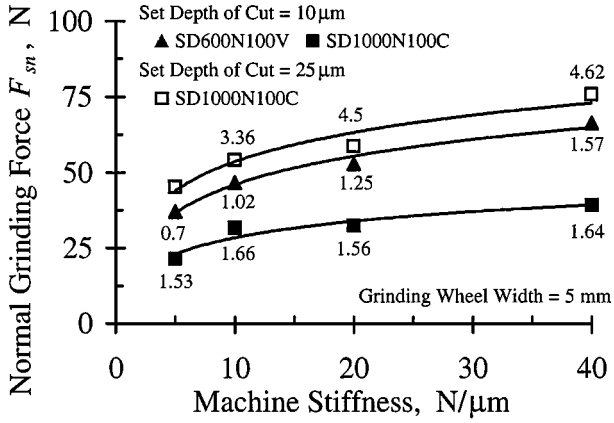

(b) SD600N100V and SD1000N100C wheels.

Figure 3 Machine stiffness versus normal grinding force F_{sn}. Measured stock removal rates, mm^3/(min·mm), are shown next to data points.

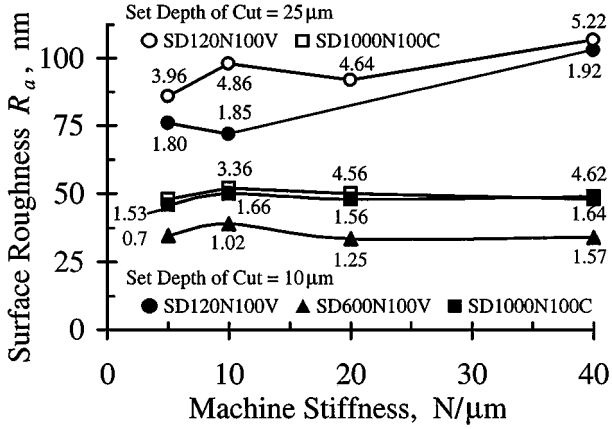

Figure 4 Machine stiffness versus surface finish R_a. Measured stock removal rates, mm^3/(min·mm), are shown next to data points.

3.2. Workpiece surface roughness

Fig. 4 shows how the workpiece surface roughness R_a changed with machine stiffness. Increasing machine stiffness yields higher stock removal rates, e.g. larger ADOCs. Mayer and Fang [13] show that as the grit depth of cut increases the surface roughness correspondingly increases. This is the general trend for the 120-V wheel curves with a mean grit size of 125 μm. However, this was not the case for the 600-V and 1000-C wheels, which have a mean grit size of 15 μm.

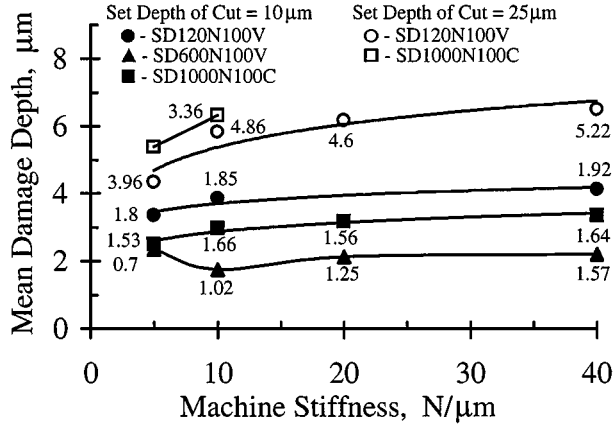

Figure 5 Machine stiffness versus measured damage depth. Measured stock removal rates, mm^3/(min·mm), are shown next to data points.

There is little change in the surface roughness as the machine stiffness is increased, although both the F_{sn} and stock removal rate increased with machine stiffness. Comparing these two wheels for a 10 μm SDOC, the surface roughness was consistently greater for the 1000-C wheel. The results for the 1000-C wheel at both SDOCs are nearly the same, although the stock removal rates were higher for the larger SDOC. This result may be due to the wheel's CIFB, where rubbing between the workpiece and bond may occur and control the grit depth of cut.

3.3. Damage depth measurements

Fig. 5 shows how the mean depth of grinding induced damage varied with machine stiffness. The damage depth curves for the 120-V and 1000-C wheels have the same general trend as the F_{sn} curves shown in Fig. 3. The workpiece damage caused by these two wheels increases slightly with machine stiffness and F_{sn}. The above trend, however, does not hold for the 600-V wheel, where an increase in damage occurred at the 5 N/μm machine stiffness data point.

In an effort to explain this variation, spectrum analysis was done on the normal grinding force data. A dominant periodic variation occurring once per revolution of the grinding wheel (42 Hz) existed for the 600-V wheel. The other two wheels showed similar harmonics, however the relative magnitude peak-to-average ratio was approximately one-third that was found for the 600-V wheel. The 600-V grinding wheel was then carefully inspected and an imperfection, a small crack, was found. The significance of this analysis reiterates that when the grinding machine operates near resonance, as is the case when the machine-loop stiffness is 5 N/μm, it becomes sensitive to periodic excitation at the frequency of the wheel rotation. Increasing the machine stiffness increases the resonant frequency of the system, making the system less sensitive to periodic disturbances at the grinding wheel rotational frequency.

Fig. 6 shows how the measured stock removal rates relate to damage depth. Each wheel is represented by a uniquely shaped symbol, in which symbol-fill gradients are used to differentiate the machine stiffnesses. The programmed specific stock removal rates

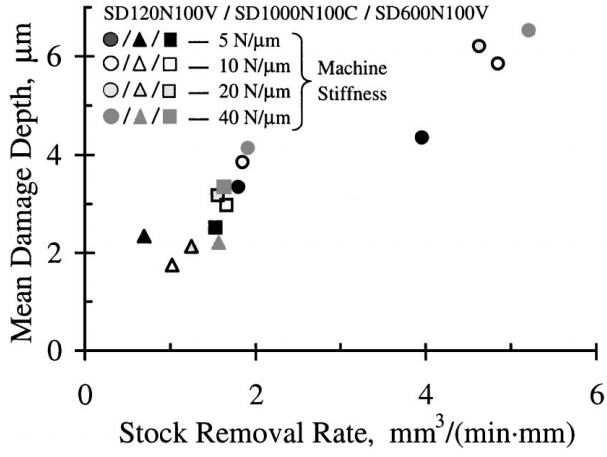

Figure 6 Stock removal rate versus damage depth.

are $Q'_w = 2.4$ mm^3/(min·mm) and $Q'_w = 6.0$ mm^3/(min·mm). In general, the measured stock removal rates approach the programmed removal rates as the machine stiffness increases. At the higher programmed rate, the influence of machine stiffness on damage depth is more apparent, as the damage depth increases with the machine stiffness. In other words, the damage depth increases with a corresponding increase in stock removal rate. The influence of machine stiffness was less profound for the lower stock removal rates, although the damage depths generally increase with machine stiffness. The close grouping of data for the 120-V and 1000-C wheels at an SDOC = 10 μm, with respect to the stock removal rate, indicates the consistency of the cutting condition. The data for the 600-V wheel indicates that as the machine stiffness increases the damage depth remains nearly constant although the stock removal rate increases.

3.4. Workpiece strength and residual stress

Fig. 7 indicates the bending strength of the ground specimens is not significantly influenced by machine stiffness, although the strength was different between each wheel. Theoretically, the strength of the ground workpieces should decrease with an increase in machine stiffness due to increasing ADOC and induced damage depth. The damage depth for the 120-V wheel is about one-and-one-half times greater between the two SDOCs, as shown in Fig. 5, although the workpiece strength was practically the same, as illustrated in Fig. 7a. The results for the 1000-C wheel, Fig. 7b, were similar to those for the 120-V wheel. The strength of the workpieces ground with the 600-V wheel was higher than the other two wheels, however the damage depth was only slightly less.

One explanation for why the workpiece strengths are not significantly affected by the damage depth may be found in the material grain structure. The grain structure of the HPSSN test material has large elongated grains with lengths between 1–8 μm and a relatively large aspect ratio of about 4, as shown in Fig. 11. Materials with this characteristic have a steeply rising toughness curve with increasing crack length as compared to

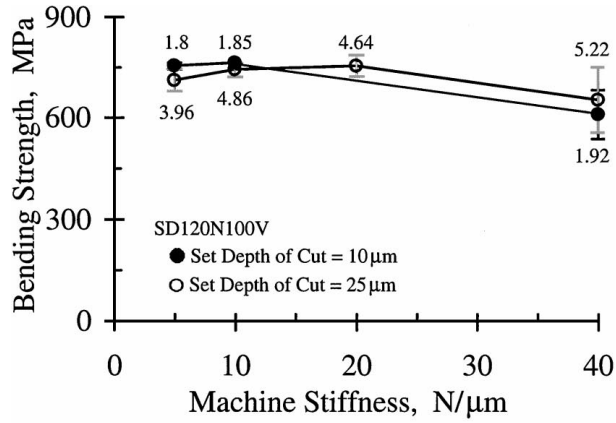

(a) SD120N100V wheel.

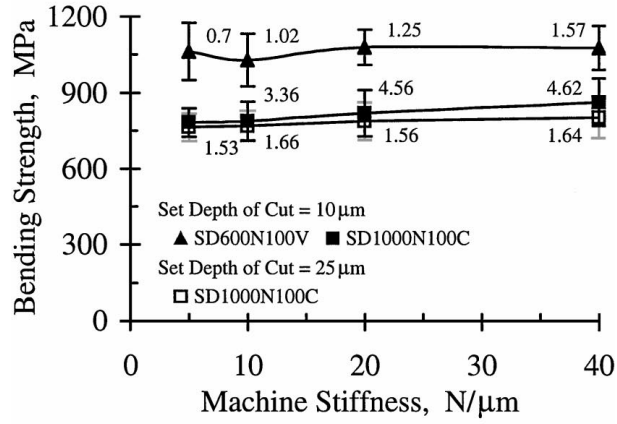

(b) SD600N100V and SD1000N100C wheels.

Figure 7 Machine stiffness versus bending strength. Measured stock removal rates, mm^3/(min·mm), are shown next to data points.

a fine-grain material [3]. According to Xu *et al.* [3], the important manifestation of a steeply rising toughness curve is material flaw tolerance, where strength becomes less sensitive to the size of flaws (or cracks) produced by machining. This is one reason why the material did not suffer a significant strength reduction for the larger damage depths.

In an effort to further explain the workpiece strength differences between the grinding wheels, residual stress measurements as well as lapping and bending tests were conducted on the as-received specimens. The bending strength of the as-received workpiece material, specified by the manufacturer, was 1051 MPa. In-house bending tests on the as-received specimens yielded a strength of 1040 MPa, which confirmed the consistency of the testing method. The mean residual stress, to a depth of 25 μm in the longitudinal direction, of eight as-received pieces was found to be compressive with a magnitude of 226 ± 75 MPa. Lapping tests were conducted to remove the residual stresses in the as-received specimens on the bending tensile stress face. The strength of specimens lapped using 6–12 μm free diamond grits was 764 ± 8 MPa, and using 0–0.25 μm grits, 846 ± 8 MPa. The surface roughness along the longitudinal direction was 160 nm for the as-received specimens, 110 nm for the specimens lapped with coarse grits and 24 nm for those lapped with fine grits.

Based on the residual stress measurements and lapping experiments conducted, it was concluded that the longitudinal direction compressive residual stress in the as-received workpieces influenced the workpiece bending strength. This was because the lapping process removed the surface residual stresses, causing the strength of the lapped specimens to be lower than the as-received strength of 1040 MPa.

To further analyze the results shown in Fig. 7, the corresponding workpiece strength, residual stress and damage depth measurements for an SDOC = 10 μm and machine stiffness of 10 N/μm are shown together with the as-received workpiece data in Fig. 8. The error bars represent one standard deviation. If the bending strength of the fine-lapped specimens is considered the baseline strength of the as-received specimens, 846 MPa indicated by the dashed line, the 120-V and 1000-C wheels yielded workpieces with approximately 10% and 7% strength reduction respectively. The 1000-C wheel induced the lowest compressive residual stress to the workpiece, and also a relatively low damage depth. However, the 120-V wheel induced the highest level of compressive residual stress and damage depth. The strength benefit of the compressive residual stress in this case is counter-balanced by the detrimental effect of the damage. The 600-V wheel, which also had a vitrified bond, resulted in a mean workpiece strength of around 1129 MPa, a 22% strength increase. The compressive residual stresses were 242 MPa, but at a low level of damage depth due to the smaller mean grit size.

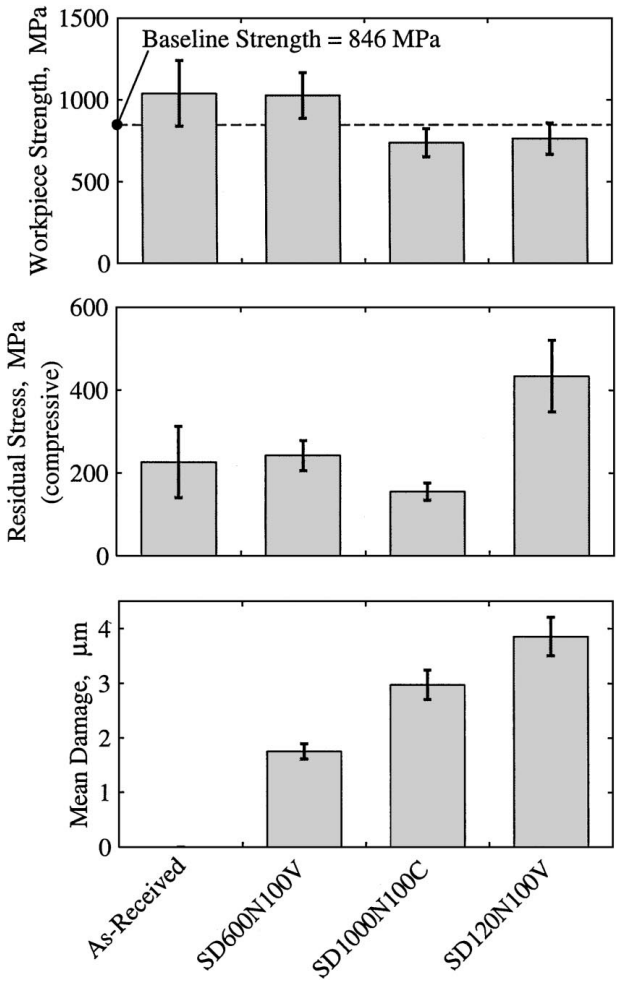

Figure 8 Workpiece strength, residual stress, and mean damage depth for SDOC = 10 μm and machine stiffness of 10 N/μm.

3.5. SEM observations

Fig. 9 shows typical ground and lapped surfaces for each grinding wheel at an SDOC = 10 μm and a

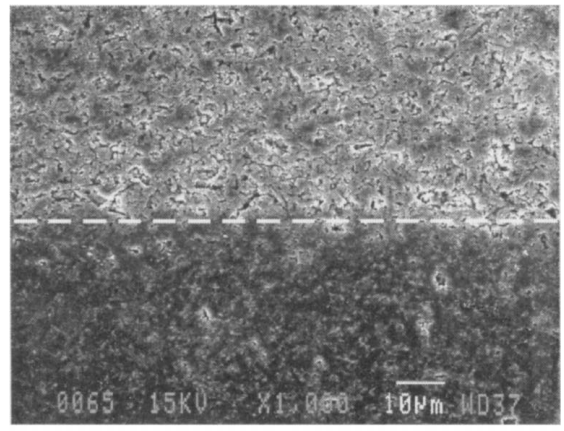

(a) SD120N100V wheel, grit size 125 μm.

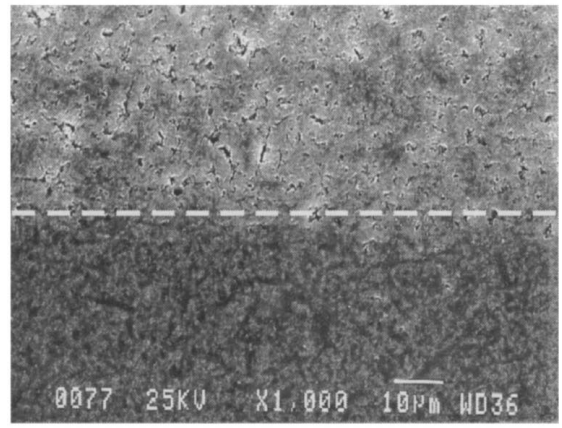

(b) SD600N100V wheel, grit size 15 μm.

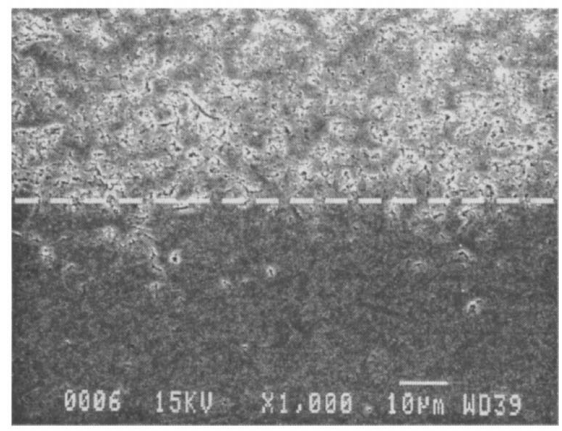

(c) SD1000N100C wheel, grit size 15 μm.

Figure 9 Comparison of ground surfaces and damage for different mean grit size wheels. The ground surface is above the dashed line and the lapped surface containing the subsurface damage is below the line. Each workpiece was ground with SDOC = 10 μm and machine stiffness of 5 N/μm.

TABLE IV SEM micrograph grinding results summary

Figure number	Grinding wheel	R_a (nm)	Damage depth, mean (μm)	F_{sn} (N)
9(a)	120-V	76.0	3.35	27.22
9(b)	600-V	34.8	2.34	36.99
9(c)	1000-C	46.0	2.51	21.38
10(a)	120-V	98.0	5.84	61.75
10(b)	120-V	106.9	6.52	71.07

machine stiffness of 5 N/μm. As illustrated in Fig. 2, the ground surface is shown above the dashed line and the taper lapped surface below the line, where the subsurface damage is revealed. The grinding-induced damage was measured with a scale relative to the dashed reference line in a perpendicular direction toward the lapped surface. Table IV shows the average measured parameters for each wheel under this grinding condition.

The ground surfaces in Fig. 9a and Fig. 9c have similar characteristics in that they are densely populated with numerous pit and void irregularities. The irregularities in Fig. 9a appear less concentrated but geometrically larger overall compared to those in Fig. 9c. The subsurface damage appearance on the lapped surface is similar between the specimens, where the most

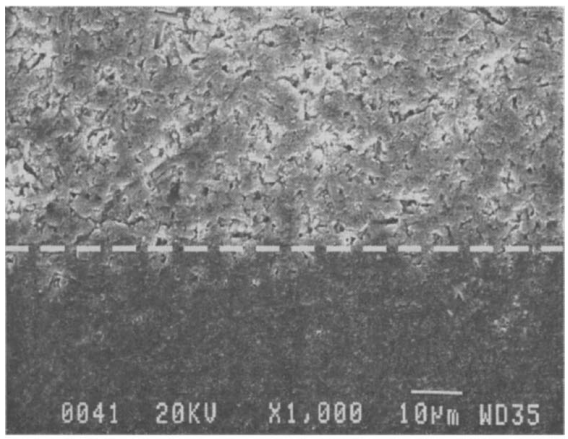

(a) Machine stiffness = 10 N/μm.

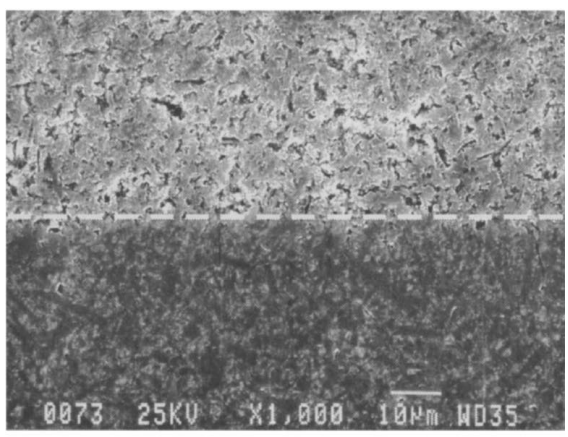

(b) Machine stiffness = 40 N/μm.

Figure 10 The effect of machine stiffness on the surface of ground silicon nitride for the SD120N100V wheel used with an SDOC of 25 μm.

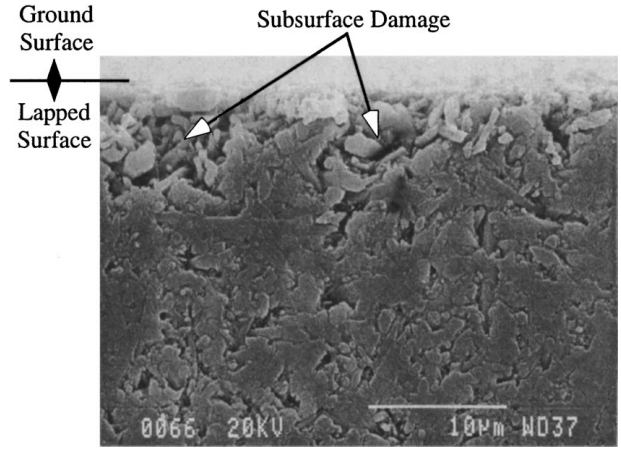

Figure 11 Side profile of etched silicon nitride workpiece ground with 120-V wheel at and SDOC = 10 μm and machine stiffness of 5 N/μm. The specimen was etched in 100°C hydrofluoric acid for 25 min.

widespread damage is shown in Fig. 9a. The micrograph for the 600-V wheel, Fig. 9b, shows a much smoother ground surface with sparse damage on the lapped surface. These images typify the measured damage depth values. The larger grit grinding wheel, 125 μm, produced a rougher surface and more damage compared to the 15 μm mean grit size wheels. The 1000-C wheel had more damage and a rougher surface compared to the 600-V wheel of the same grit size. The ELID system maintained the wheel sharpness throughout the grinding cycle.

Fig. 10 illustrates the effect of machine stiffness on subsurface damage and ground surface characteristics for the 120-V wheel used with an SDOC = 25 μm. Fig. 10a shows the results for a machine stiffness of 10 N/μm while Fig. 10b shows the results for a stiffness of 40 N/μm. Table IV shows the average values of the measured parameters. The ground surface appears slightly rougher for the higher stiffness while the damage depths appear similar. In both cases, the lapped surfaces have few scratches and the transition between the ground and lapped surfaces is apparent.

Fig. 11 shows the side profile of a specimen etched in 100°C hydrofluoric acid for 25 min. The top surface was ground with the 120-V wheel at an SDOC = 10 μm and machine stiffness of 5 N/μm. The indicated grinding-induced subsurface damage is about 8 μm. The large elongated grain structure can be observed with grain lengths between 1–8 μm and an aspect ratio of about 4. The grain size characteristics are related to the material toughness and resistance to strength loss resulting from grinding-induced damage.

4. Conclusions

The experimental results indicate the grinding wheel bond and grit size influence the grinding forces, surface roughness, damage depth and bending strength of silicon nitride workpieces. All workpieces had grinding damage and measurable residual stresses, which do not seem to be limited to severely damaged surfaces. The grinding machine stiffness has an insignificant effect on the workpiece flexural strength, but rather

influences the depth of cut. Machine-loop stiffnesses as low as 5 N/μm can be used for single-pass ceramic grinding; however, the grinding efficiency and accuracy are reduced. A stiffer grinding machine has advantages over a less stiff machine, with respect to accuracy, because the ADOC approaches the SDOC as the stiffness is increased.

Compressive residual stress can effectively increase workpiece strength. However, this benefit can be countered by the deleterious effect of grinding-induced damage. The strength of ground ceramic workpieces is determined by the material baseline strength, the grinding-induced compressive residual stress and grinding-induced damage. The workpiece strengths in this study were both higher and lower than that of the bulk material. Grinding-induced residual stress depends on the wheel bond type and abrasive grit size. A finer grit wheel can be used to improve both surface finish and strength. In general, more compressive residual stress can be induced with a dull grinding wheel, or a wheel with a large grit size, or a wheel with a stiff and strong bond material. Less damage will be generated by using a small grit depth of cut and a high-concentration grinding wheel.

The ELID-CIFB wheel system out-performed the vitrified bond wheels in maintaining stock removal rates throughout the grinding cycle, resulting in more consistent workpiece surface conditions and uniform damage depth measurements. However, the CIFB wheel yields a rougher surface finish and lower bending strength compared with a vitrified bond wheel with the same grit size. The CIFB wheel bond matrix apparently controls the penetration of the grit rather than the machine structure, as was the case for the vitrified bond wheels. This is revealed through the consistent surface roughness results for different depths of cut. Therefore, the combination of a very high static machine stiffness and large depth of cut for the CIFB wheel might be deleterious to the workpiece integrity because very high rubbing forces can build up between the bond matrix and the workpiece material.

Grinding should be performed with a wheel rotational speed away from the machine natural frequency and its harmonics. The grinding machine becomes increasingly sensitive to a once-per-revolution disturbance when the wheel rotational speed harmonic approaches a grinding machine resonance. This phenomenon was illustrated by a small defect in the 600-V wheel, which influenced the surface roughness, damage depth and workpiece strength results for a machine stiffness of 5 N/μm. The other two wheels tested showed no signs of a periodic disturbance.

The depth of grinding-induced damage was effectively assessed using a taper polishing method and SEM. A high degree of confidence was realized in determining the transition between the ground and lapped surfaces as well as the assessment of damage versus material flaws.

Acknowledgements

The authors gratefully acknowledge the support by the Department of Energy under contract #19X-SU366C with the Lockheed Martin Energy Research Corporation, and by the U.S. National Science Foundation under grant DMI-9500223. Appreciation is also owed undergraduate students Mr. Khon Lam and Mr. Hoang Phung for their assistance in the experimentation.

References

1. YOSHIO ICHIDA and KOZO KISHI, *Annals of the CIRP* **42**(1) (1993) 647.
2. R. KOMANDURI, *ibid.* **45**(1) (1996) 509.
3. HOCKIN H. K. XU, SAID JAHANMIR and LEWIS K. IVES, *Journal of Materials Research* **11**(7) (1996) 1717.
4. BI ZHANG, HITOSHI TOKURA and MASANORI YOSHIKAWA, *Journals of The Japan Society of Precision Engineering* **54**(8) (1988) 1537. Written in Japanese.
5. MASANORI YOSHIKAWA, BI ZHANG and HITOSHI TOKURA, *Journal of the Ceramic Society of Japan, International Edition* **95** (1987) 911.
6. BI ZHANG and TREVOR D. HOWES, *Annals of the CIRP* **43**(1) (1994) 305.
7. *Idem.*, *ibid.* **44**(1) (1995) 263.
8. D. JOHNSON-WALLS, A. G. EVANS, D. B. MARSHALL and M. R. JAMES, *Journal of the American Ceramic Society* **69**(1) (1986) 44.
9. S. MALKIN and T. W. HWANG, *Annals of the CIRP* **45**(2) (1996) 569.
10. NOBORU MORITA, TAKEHIRO WATANABE and YOSHITARO YOSHIDA, *JSME International Journal, Series III* **35**(4) (1992) 667.
11. B. EIGENMANN, B. SCHOLTES and E. MACHERAUCH, *Materials Science and Engineering*, **A118** (1989) 1.
12. H. K. TÖNSHOFF, H. TRUMPOLD, E. BRINKSMEIER and H. G. WEBKER, *Annals of the CIRP* **38**(2) (1989) 699.
13. JOHN E. MAYER, JR. and GWO-PING FANG, *Transactions of NAMRI/SME, XXII* (1994) 187.
14. P. ROTH, H. G. WOBKER and C. MENZ, *Tribology Transactions*, **38**(3) (1995) 714.
15. TIMOTHY J. STRAKNA, SAID JAHANMIR, RICHARD L. ALLOR and KRIS V. KUMAR, *Transactions of NAMRI/SME, XXIII* (1995) 85.
16. HOCKIN H. K. XU, LANHUA WEI and SAID JAHANMIR, *Journal of Materials Research* **10**(12) (1995) 3204.
17. K. KITAJIMA, G. Q. CAI, N. KUMAGAI, Y. TANAKA and H. W. ZENG, *Annals of the CIRP* **41**(1) (1992) 367.
18. R. KOMANDURI, D. A. LUCCA and Y. TANI, *Annals of the CIRP* **46** (1997) 1. Keynote Paper, STC G.
19. JOHN E. MAYER, JR. and GWO-PING FANG, In 1st International Machining and Grinding Conference, Machining Technology Association of SME, Dearborn, Michigan, September 1995, p.153.
20. JOHN E. MAYER, JR. and GWO-PING FANG, *Annals of the CIRP* **44**(1) (1995) 279.
21. K. SUBRAMANIAN, P. D. REDINGTON and S. RAMANATH, *American Ceramic Society Bulletin*, **73**(3) (1994) 61.
22. G. WARNECKE, U. ROSENBERGER and J. MILBERG, *Annals of the CIRP* **44**(1) (1995) 283.
23. Uwe Rosenberger and Guenter Warnecke, *Transactions of NAMRI/SME, XXII* (1994) 179.
24. BI ZHANG, FULUN YANG, JIEXIN WANG, ZHENQI ZHU and RICHARD MONAHAN, "Transactions of the North American Manufacturing Research Institution of SME," Georgia Institute of Technology, Atlanta, GA, May 1998 (Society of Manufacturing Engineers) Vol. XXVI, p. 273.
25. K. R. MCKINNEY and R. W. RICE, "Fracture Mechanics for Ceramics, Rocks, and Concrete, National Bureau of Standards," Vol. 1, edited by S. W. Freiman and E. R. Fuller, Jr. (American Society for Testing and Materials, Philadelphia, 1981) P. 118.
26. R. W. RICE, "Fracture Mechanics for Ceramics, Rocks, and Concrete, National Bureau of Standards," Vol. 1, edited by S. W. Freiman and E. R. Fuller, Jr. (American Society for Testing and Materials, Philadelphia, 1981) p. 96.
27. *Idem.* or *Id.*, Machining of Advanced Materials, Proceedings of the International Conference on Machining of Advanced Materials,

Vol. 847 (NIST Special Publication, US Government Printing Office, Washington DC, July 1993) p. 185.
28. HYO-SOK AHN, LANHUA WEI and SAID JAHANMIR, *ASME Journal of Engineering Materials and Technology*, **118**(3) (1996) 402.
29. HOCKIN H. K. XU and SAID JAHANMIR, *J. Amer. Ceram. Soc.*, **77**(5) (1994) 1388.
30. CHANGSHEN GUO and RONALD H. CHAND, In 1st International Machining and Grinding conference, Machining Technology Association of SME, Dearborn, Michigan, September 1995, p. 125.
31. ASTM, Standard Test Method for Flexure Strength of Advanced Ceramics at Ambient Temperature. *American Society for Testing and Materials*, **C1161**(94) (1994) 309.

Received 15 April
and accepted 19 August 1999